Journal of Power Sources 533 (2022) 231383

Contents lists available at ScienceDirect

Journal of Power Sources

journal homepage: www.elsevier.com/locate/jpowsour

Establishing substitution rules of functional groups for high-capacity organic anode materials in Na-ion batteries

Kathryn Holguin [a,1], Kaiqiang Qin [a,1], Ethan Phillip Kamphaus [b], Fu Chen [c], Lei Cheng [b,**], Gui-Liang Xu [d,***], Khalil Amine [d,e], Chao Luo [a,f,*]

[a] Department of Chemistry and Biochemistry, George Mason University, Fairfax, VA, 22030, USA
[b] Materials Science Division, Argonne National Laboratory, Lemont, IL, 60439, USA
[c] Department of Chemistry and Biochemistry, University of Maryland, College Park, MD, 20742, USA
[d] Chemical Sciences and Engineering Division, Argonne National Laboratory, Lemont, IL, 60439, USA
[e] Materials Science and Engineering, Stanford University, Stanford, CA, 94305, USA
[f] Quantum Science & Engineering Center, George Mason University, Fairfax, VA, 22030, USA

HIGHLIGHTS

- N substituted carboxylates are exploited as anode materials in Na-ion batteries.
- Impacts of N substitution and conjugation structure to performance are explored.
- N-doped reduced graphene oxide is used to enhance the electrochemical performance.
- All-organic Na-ion full cells have been demonstrated.
- Substitution rules of functional groups in carboxylate anodes are discussed.

GRAPHICAL ABSTRACT

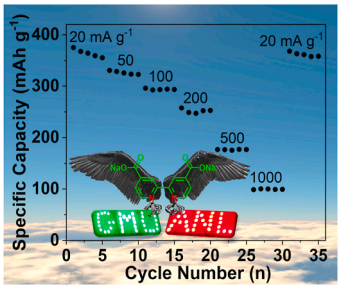

ARTICLE INFO

Keywords:
Sodium carboxylate
Organic electrode materials
Na-ion batteries
Anode
Substitution rules

ABSTRACT

Tailoring molecular structures of organic electrode materials (OEMs) can enhance their performance in Na-ion batteries, however, the substitution rules and the consequent effect on the specific capacity and working potential remain elusive. Herein, by examining three sodium carboxylates with selective N substitution or extended conjugation structure, we exploited the correlation between structure and performance to establish substitution rules for high-capacity OEMs. Our results show that substitution position and types of functional groups are essential to create active centers for uptake/removal of Na^+ and thermodynamically stabilize organic structures. Furthermore, rational host design and electrolytes modulation were performed to extend the cycle life to 500 cycles. A full cell based on the optimal 2,2′-bipyridine-4,4′-dicarboxylic acid disodium salt anode and the polyaniline cathode is demonstrated to confirm the feasibility of achieving all-organic batteries. This work provides a valuable guideline for the design principle of high-capacity and stable OEMs for sustainable energy storage.

* Corresponding author. Department of Chemistry and Biochemistry, George Mason University, Fairfax, VA, 22030, USA.
** Corresponding author.
*** Corresponding author.
E-mail addresses: leicheng@anl.gov (L. Cheng), xug@anl.gov (G.-L. Xu), cluo@gmu.edu (C. Luo).
[1] These authors contributed to this work equally.

https://doi.org/10.1016/j.jpowsour.2022.231383
Received 18 January 2022; Received in revised form 14 March 2022; Accepted 28 March 2022
Available online 3 April 2022

1. Introduction

Due to the vast demands for smart electronic devices, electric vehicles, and grid-scale electrical energy storage, it is of paramount significance to develop cost-effective and sustainable energy storage devices. Among various rechargeable batteries, Na-ion batteries (NIBs) stand out as promising alternatives to state-of-the-art lithium-ion batteries (LIBs), because of the abundance of sodium resources versus scarce lithium [1–6]. To further reduce the battery cost and mitigate the global material supply chain challenges, it is critical to eliminate the use of strategic elements (e.g. Ni, Co, Li, etc.) in the electrode materials. To this end, organic electrode materials (OEMs) offer numerous opportunities owing to the lightweight (C, H & O), low cost, abundance, high sustainability, and high recyclability [7–9].

To date, there are five types of reaction mechanisms in the organic NIBs, including carbonyl (C=O), imine (C=N), azo (N=N), thioketone/thioester (C=S), and anion insertion reactions [10–17]. The quinone-based carbonyl reaction, pyrazine-based imine reaction, and anion insertion reaction provide relatively higher reaction potentials in organic cathodes [18–22]. Nevertheless, most of the reported organic cathode materials lack Na ions, so they are not suitable as cathodes for the rocking-chair type NIBs [23–27]. The carboxylate-based carbonyl reaction, Schiff base-based imine reaction, and azo reaction can provide relatively lower reaction potentials and are thus promising candidates for NIB anodes [28–34]. The redox potentials of azo compounds are centered at ~1.3 V in NIBs [35], while imine-based polymers such as polymeric Schiff bases show redox plateaus at potentials >0.5 V [13,14]. Among various organic anodes, the carboxylate compounds are the most promising ones because of their reasonable redox potential (<0.5 V) and high specific capacity (>200 mAh g^{-1}). Due to the abundant and diverse nature of carboxylate compounds, their molecular structures can be manipulated to optimize the electrochemical performance as anodes for sustainable NIBs.

However, OEMs generally exhibit low electronic conductivity, resulting in low utilization of active material during electrochemical reactions [36]. Moreover, previous studies have shown that OEMs also suffer from high solubility in the organic electrolytes, leading to rapid capacity fading during long-term cycling [37]. To address these challenges, a common approach is to integrate OEMs with host materials that exhibit high electronic conductivity and excellent adsorption/confinement effect, for example, graphene/carbon nanotubes [38,39]. This strategy not only shortens the charge transfer pathway, but also reduces the OEMs dissolution, leading to significantly improved reaction kinetics and suppressed self-discharge phenomenon. It has been widely shown that molecular engineering of OEMs by extending the conjugated structures can simultaneously increase the electronic conductivity and improve the interaction with the carbon-based hosts due to the increased π-aromatic conjugation [40–44]. However, how the extended conjugation structure impacts the specific capacity and working voltage of OEMs remains elusive and even contradictory. For example, Wang et al. compared the performance of disodium terephthalate and sodium 4,4′-stilbene-dicarboxylate (SSDC) in NIBs to exploit the impact of extended π-conjugated structure [45]. Their results indicate that the extended π-conjugated structure increases the reversible capacity and elevates the redox potentials of carboxylate compounds. However, Abouimrane et al. explored the performance of disodium terephthalate and 1,4,5,8-naphthalenetetracarboxylate, demonstrating that the extended π-conjugated structure reduces the reversible capacity but retains the redox potentials [46]. Such conflicting results have indicated an urgent need to understand and establish rational substitution rules for the conjugated carboxylate anode materials to attain high specific capacity and reasonable working potential simultaneously.

Herein, we have tailored the molecular structures of conjugated sodium carboxylates and revealed the effect of selective substitution of N atoms in the aromatic structure and extended conjugation structure in carboxylate compounds when serving as anode materials for NIBs. Scheme 1a-c shows the molecular structures of biphenyl-3,3′-dicarboxylic acid disodium salt ($Na_2C_{14}H_8O_4$), 2,2′-bipyridine-4,4′-dicarboxylic acid disodium salt ($Na_2C_{12}H_6N_2O_4$, Na-DCA), and bicinchoninic acid disodium salt ($Na_2C_{20}H_{10}N_2O_4$), respectively. Each of them contains two carboxylate groups. Our result shows that $Na_2C_{14}H_8O_4$, without N atoms, is electrochemically inactive in NIBs because it can only form a free radical intermediate and cannot be further converted to a stable sodiated product (Scheme 1d). In sharp contrast, the presence of two pyridine ring structures in the Na-DCA could increase the available active sites and provide resonance stability during insertion/de-insertion of Na-ions (Scheme 1e), thus enabling four sodium-ion storage and a high specific capacity for Na-DCA. The contrast in electrochemical behaviors between $Na_2C_{14}H_8O_4$ and Na-DCA was additionally investigated via ab-initio simulations. The thermodynamics of Na^+ intercalation and reduction were determined from gas-phase molecular models. In the case of $Na_2C_{14}H_8O_4$, a stable structure cannot be achieved for the reduced molecule because despite every attempt used (including directly assigning the additional electrons to the molecule instead of Na^+ ions), a different optimized structure would be obtained. For instance, the Na-ions would be reduced instead of the molecule. This is indicative that the reaction as drawn in Scheme 1f is highly unfavorable or else the structure would have been optimized given the strict input constraints utilized. This confirms the experimental evidence that $Na_2C_{14}H_8O_4$ is electrochemically inactive. On the contrary, both the first and second steps of the reaction of Na-DCA were determined to be thermodynamically favorable (Scheme 1g). The first step is associated with a ΔG of −0.72 eV and the second step's $\Delta G = -0.83$ eV, demonstrating the four sodium-ion storage mechanism. Therefore, this work unveils the substitution rule of introducing N onto the *para* position of the benzene ring bearing carboxylate groups to promote the thermodynamic reaction in NIBs.

In addition to the experimental and computational studies for $Na_2C_{14}H_8O_4$ and Na-DCA, we further extended the conjugation structure of Na-DCA to form $Na_2C_{20}H_{10}N_2O_4$, which showed a decreased specific capacity and an increased redox potential. Moreover, we further integrated Na-DCA with nitrogen-doped reduced graphene oxide (NrGO) to enhance the conductivity, mitigate the solubility of Na-DCA, and accommodate the volume change through the π-π interaction between the conjugated structures. The results showed that the Na-DCA-NrGO anode exhibits a high specific capacity of >300 mAh g^{-1} at 50 mA g^{-1} and a pair of redox plateaus centered at ~0.48 V together with superior capacity retention up to 500 cycles, demonstrating exceptional electrochemical performance. An all-organic full cell based on a Na-DCA-NrGO anode and a polyaniline cathode is also demonstrated to promote the practical application of the sodium carboxylate anode.

2. Experimental

2.1. Synthesis/preparation of electrode materials

2,2′-bypyridine-4,4′-dicarboxylic acid disodium salt (Na-DCA/$Na_2C_{12}H_6N_2O_4$) was prepared as follows: 2,2′-bypyridine-4,4′-dicarboxylic acid (Alfa Aesar, 98%) was dispersed in ethanol with sodium hydroxide pellets (Alfa Aesar, 99%) in 5% excess. The solution was stirred at room temperature for 24 h, then the solution was filtered to collect the precipitate. The precipitate was washed with ethanol and dried in the vacuum oven at 90 °C overnight. The isolated product was a white powder.

2.2. Materials characterization

Fourier transform infrared spectroscopy (FTIR) was recorded by Agilent Cary 630 FTIR Spectrometer; Nuclear magnetic resonance (NMR) was recorded by Bruker Ascend 400; X-ray diffraction (XRD) pattern was recorded by Rigaku MiniFlex using CuKα radiation; and SEM images were taken by Hitachi SU-70 analytical ultra-high-

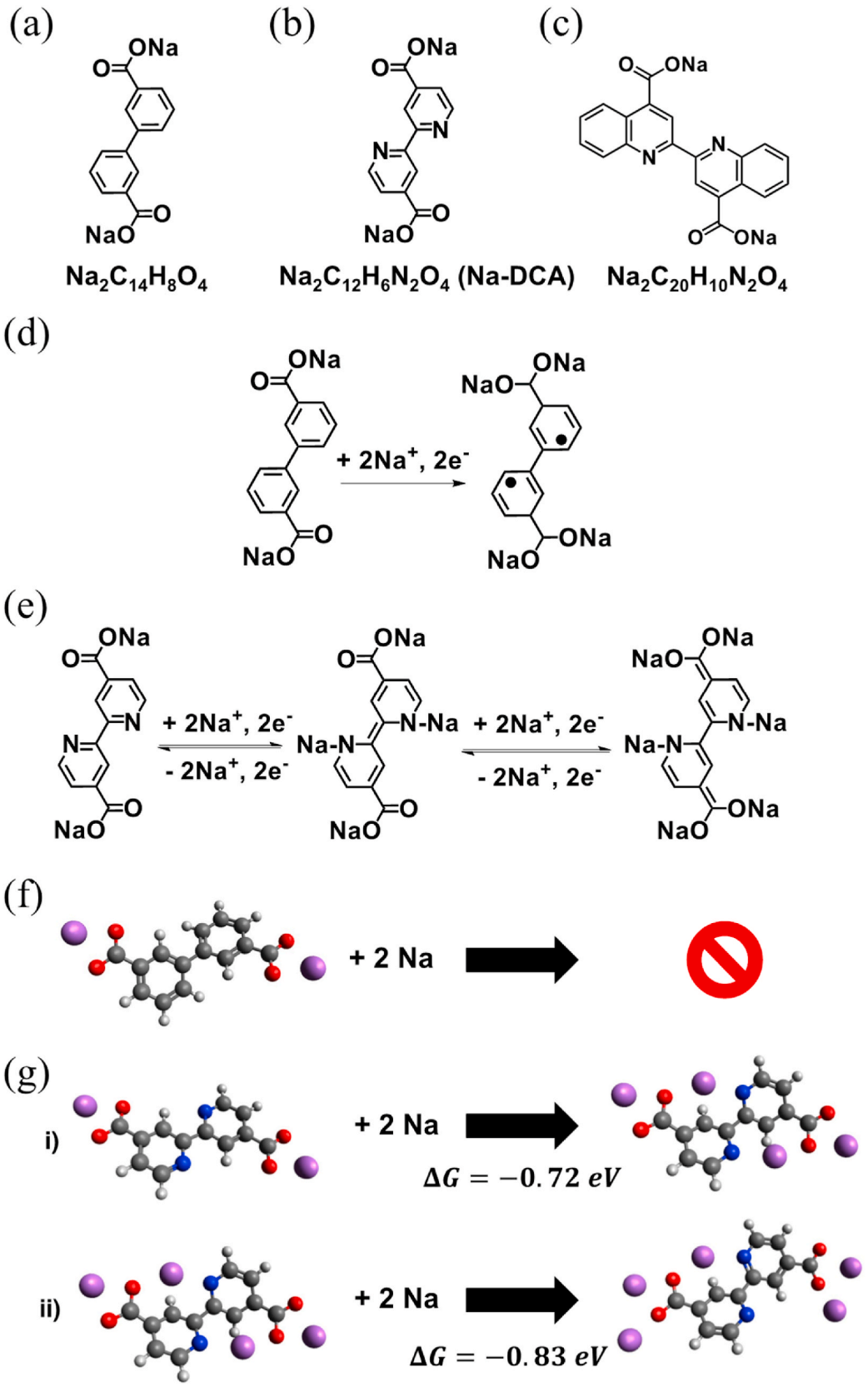

Scheme 1. The molecular structures of the three sodium carboxylates; (a) $Na_2C_{14}H_8O_4$, (b) $Na_2C_{12}H_6N_2O_4$ (Na-DCA), and (c) $Na_2C_{20}H_{10}N_2O_4$; and the sodiation/de-sodiation mechanisms of (d) $Na_2C_{12}H_8O_4$ and (e) Na-DCA; Density functional theory calculations for the electrochemical reaction of (f) $Na_2C_{12}H_8O_4$ with Na^+, and (g) Na-DCA with Na^+.

resolution SEM (Japan) and Joel JSM-IT500HR/LV high-resolution SEM. Solid-state natural abundance ^{13}C and ^{15}N NMR spectra of magic angle spinning (MAS) samples were acquired on a Bruker AVANCE NEO 500 MHz NMR spectrometer using the combination of standard cross-polarization (CP) with proton spinal-64 decoupling. Samples were packed in 3.2 mm o.d. rotors and run in a Bruker double-resonance magic-angle spinning (MAS) probe. Proton 90° pulse widths of 2.5 μs, contact times of 2 ms, and pulse delays of 5 s were used to acquire both ^{13}C and ^{15}N NMR spectra. Carbon-13 chemical shifts were referenced with respect to TMS by setting $\delta(^{13}C) = 0$ ppm and nitrogen-15 chemical shifts were referenced with respect to α-glycine by setting $\delta(^{15}N) = 33.4$ ppm. Spectra of MAS samples were acquired at ambient temperature with spinning frequencies of 8–10 kHz and spinning sidebands were confirmed by running experiments with a different spinning rate. ^{13}C CP/MAS NMR spectra were acquired with a total scan of 4k and ^{15}N CP/MAS NMR spectra were acquired with a total scan of 90k.

2.3. Electrode fabrication and battery assembly

The reference materials, biphenyl-3,3′-dicarboxylic acid disodium salt ($Na_2C_{14}H_8O_4$) and bicinchoninic acid disodium salt ($Na_2C_{20}H_{10}N_2O_4$), were each mixed with carbon black (CB) and sodium alginate (SA) binder to form a slurry with a weight ratio of 60:30:10. The electrode was prepared by casting the slurry onto copper foil using a doctor blade and dried in a vacuum oven at 90 °C overnight. The slurry coated on copper foil was punched into circular electrodes ($Na_2C_{14}H_8O_4$ and $Na_2C_{20}H_{10}N_2O_4$, respectively) with a mass loading of ~1.2 mg cm^{-2} based on the active material. Coin cells for Na-ion batteries (NIBs) were assembled using sodium metal as the counter electrode, 1.2 M $NaClO_4$ in ethylene carbonate/diethyl carbonate (EC/DEC) (1:1 by volume) electrolyte, and glass fiber (Whatman) as the separator.

The 2,2′-bypyridine-4,4′-dicarboxylic acid disodium salt (Na-DCA/$Na_2C_{12}H_6N_2O_4$) was mixed with carbon black (CB) and sodium alginate (SA) binder to form a slurry with a weight ratio of 60:30:10. The electrode was prepared by casting the slurry onto copper foil using a doctor blade and dried in a vacuum oven at 90 °C overnight. The slurry coated on copper foil was punched into circular electrodes (Na-DCA) with a mass loading of ~1.2 mg cm^{-2} based on the active material. Coin cells for Na-ion batteries (NIBs) were assembled using sodium metal as the counter electrode, 1.0 M and 1.2 M $NaClO_4$ in ethylene carbonate/diethyl carbonate (EC/DEC) (1:1 by volume) electrolyte, and glass fiber (Whatman) as the separator.

The 2,2′-bypyridine-4,4′-dicarboxylic acid disodium salt (Na-DCA/$Na_2C_{12}H_6N_2O_4$) was mixed with nitrogen-doped reduced graphene oxide (NrGO, ACS Material, LLC, Single layer graphene, N-doped Powder, 1g) in a 2:1 ratio and hand-ground for 1 h. This subsequent mixture was then mixed with carbon black (CB) and sodium alginate (SA) binder to form a slurry with a weight ratio of 80:10:10. The electrode was prepared by casting the slurry onto copper foil using a doctor blade and dried in a vacuum oven at 90 °C overnight. The slurry coated on copper foil was punched into circular electrodes (Na-DCA-NrGO) with a mass loading of ~1.2 mg cm^{-2} based on the active material. Coin cells for Na-ion batteries (NIBs) were assembled using sodium metal as the counter electrode, 1.0 M and 1.2 M $NaClO_4$ in ethylene carbonate/diethyl carbonate (EC/DEC) (1:1 by volume) electrolyte, and glass fiber (Whatman) as the separator. For the full cell assembly, the PANI cathode and Na-DCA/$Na_2C_{12}H_6N_2O_4$ anode were each mixed with NrGO in a 2:1 ratio, mixed with CB and SA in the mass ratio of 80:10:10, and the resulting slurry was cast onto aluminum foil using a doctor blade and dried in a vacuum oven at 90 °C overnight. The slurry coated on aluminum foil was punched into circular electrodes, PANI-NrGO and Na-DCA-NrGO, respectively, with a 2:1 mass loading ratio of ~2.4 mg cm^{-2} (cathode): ~1.2 mg cm^{-2} (anode) based on the active material, respectively.

2.4. Electrochemical measurements

All galvanostatic discharge-charge cycles were performed using an Arbin battery testing instrument (Arbin Instrument, model LBT20084) at room temperature in a voltage range of 0.1–2.0 V. Specific capacity is calculated based on the mass of active material in the composite anode. Cyclic voltammograms (CVs) were recorded using Gamry Reference 1010E Potentiostat/Galvanostat/ZRA with a scan rate of 0.1–1.0 mV s^{-1}. Impedance analysis was also performed by Gamry Reference 1010E Potentiostat/Galvanostat/ZRA. CVs at various scan rates were used to study the reaction kinetics of Na-DCA (Na-DCA-NrGO/NrGO-$Na_2C_{12}H_6N_2O_4$) anode in NIBs. For the assembly of the Na-DCA-NrGO|PANI-NrGO full cell, the Na-DCA-NrGO/NrGO-$Na_2C_{12}H_6N_2O_4$ anode and PANI-NrGO cathode were pre-cycled at 100 mA g^{-1} in a half cell for 15 cycles and were then disassembled in a glovebox after charging to 2 V and discharging to 2 V, respectively. The pre-sodiated Na-DCA-NrGO/NrGO-$Na_2C_{12}H_6N_2O_4$ anode and PANI-NrGO cathode were reassembled in a full cell and cycled at room temperature in a voltage range of 0.5–3.9 V. After cycling, cyclic voltammograms (CVs) were recorded using Gamry Reference 1010E Potentiostat/Galvanostat/ZRA with a scan rate of 0.1–1.0 mV s^{-1}.

2.5. Computational methodology

All gas-phase molecular simulations were carried out with the software package Gaussian 16. The B3LYP hybrid density functional theory (DFT) level of theory was used with the 6–311++G(d,p) split valence basis set with added polarization and diffuse functions. The molecules of interest underwent a geometry optimization to find the most stable and expected structures (including screening different possible spin multiplicities) followed by a frequency calculation to determine the vibrational, rotational, and translational contributions to the free energy. All free energy calculations were carried out at 298 K. To ensure that the molecules were receiving the additional electrons in the reduced simulations, the fragment input specification was used to attempt to ensure this outcome.

3. Results and discussion

To investigate the electrochemistry of the nitrogen-containing sodium carboxylate in NIBs, we synthesized Na-DCA and the other two control samples ($Na_2C_{14}H_8O_4$ and $Na_2C_{20}H_{10}N_2O_4$). The structures of the resulting organic salts were confirmed and characterized by X-ray powder diffraction (XRD), Fourier-transform infrared (FTIR) spectroscopy, proton nuclear magnetic resonance (^1H NMR), carbon-13 nuclear magnetic resonance (^{13}C NMR), solid-state NMR, and scanning electron microscopy (SEM). As shown in Fig. 1a (black), S1a, and S2a, all three materials exhibit crystalline structures. The FTIR spectra for the three compounds in Fig. 1b (black), S1b, and S2b, show C=O asymmetric vibration peaks for Na-DCA, $Na_2C_{14}H_8O_4$, and $Na_2C_{20}H_{10}N_2O_4$ at 1610 cm^{-1}, 1677 cm^{-1}, and 1580 cm^{-1}, respectively, and symmetric vibrational peaks at 1394 cm^{-1}, 1300 cm^{-1}, and 1362 cm^{-1}, respectively. New peaks can be observed at 1610 cm^{-1} and 1394 cm^{-1}, corresponding to asymmetrical and symmetrical vibrations of C=O in the carboxylates, while the peak at 1548 cm^{-1} corresponds to the vibrations of C=N in the pyridine moieties of Na-DCA. These peaks are shown in detail in Fig. S3a. Further characterizations for Na-DCA using ^1H NMR (Fig. 1c) and ^{13}C NMR (Fig. 1d) with D_2O as the solvent were obtained. In Fig. 1c, three ^1H NMR peaks in the range from 7.8 to 8.8 ppm represent the protons in the pyridine moieties of Na-DCA. There is an obvious peak at 4.790 ppm, corresponding to the chemical shift of H in the D_2O solvent. The ^{13}C NMR spectrum of Na-DCA (Fig. 1d) shows three peaks at 121.2 ppm, 123.2 ppm, and 149.6 ppm, corresponding to sp^2 carbons in the pyridine ring bonded with protons, while the peak at 146.3 ppm corresponds to sp^2 carbons in the pyridine ring bonded to the carboxylate groups. The ^{13}C NMR peak at 155.6 ppm corresponds to sp^2 carbons in

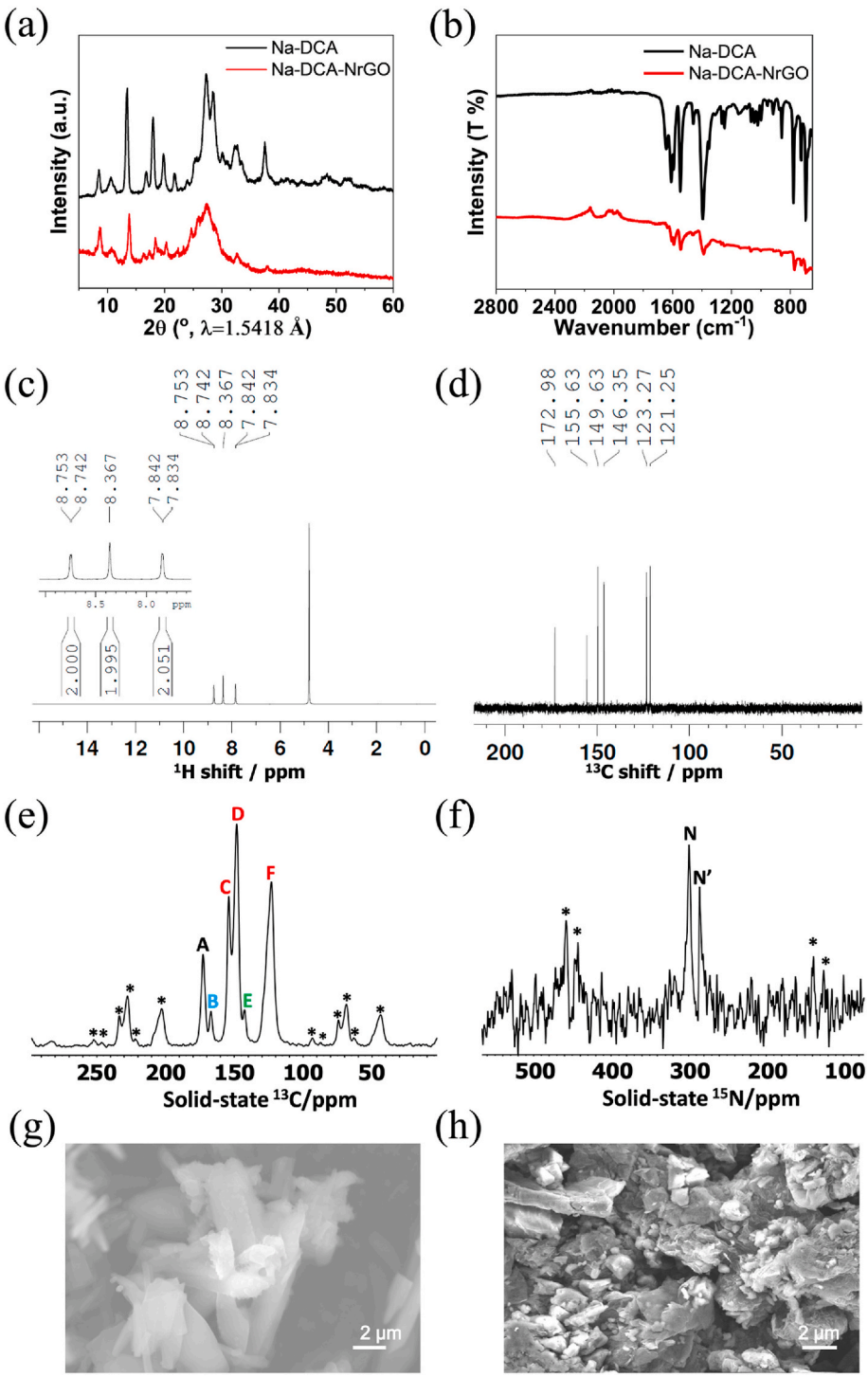

Fig. 1. Material characterizations of 2,2′-bypyridine-4,4′-dicarboxylic acid disodium salt (Na-DCA) and 2,2′-bypyridine-4,4′-dicarboxylic acid disodium salt-NrGO (Na-DCA-NrGO). (a) XRD pattern; (b) FTIR spectrum; (c) liquid-state ^{1}H NMR spectrum; (d) liquid-state ^{13}C NMR spectrum; (e) solid-state ^{13}C NMR spectrum; (f) solid-state ^{15}N NMR spectrum; and SEM images with scale bars of 2 μm of (g) Na-DCA and (h) Na-DCA-NrGO.

the pyridine rings bonded to each other, while the ^{13}C NMR peak at 172.9 ppm corresponds to sp^2 carbons in the carboxylate groups. Solid-state ^{13}C NMR and ^{15}N NMR tests were also performed to further confirm the molecular structure of Na-DCA. ^{13}C CP/MAS NMR spectrum (Fig. 1e) indicates that there are six carbon peaks with chemical shifts for ^{13}C: A – 172.7 ppm; B – 167.0 ppm; C – 154.1 ppm; D – 148.0 ppm; E – 142.6 ppm; F – 123.1 ppm. C/D/F refers to three sp^2 carbons in the pyridine ring bonded with protons. The strong ^{13}C peak intensities in C/D/F compared to those in A/B/E are due to the stronger ^{1}H–^{13}C dipolar interactions in C/D/F using CP pulse sequence. * refers to spinning sidebands. ^{15}N CP/MAS NMR spectrum (Fig. 1f) indicates that there are two nitrogen sites: the chemical shift for ^{15}N is 299.2 ppm, and the chemical shift for ^{15}N' is 285.7 ppm. The observance of two nitrogen peaks is due to the spatial asymmetrical structure of Na-DCA. * refers to spinning sidebands. The ^{1}H NMR and ^{13}C NMR spectra for $Na_2C_{14}H_8O_4$ and $Na_2C_{20}H_{10}N_2O_4$ are shown in Figs. S1c–d and S2c-d, which also confirm their molecular structures. The morphology of each compound was investigated by SEM and are shown in Fig. 1g, S1e-f, and S2e-f. Na-

DCA consists of aggregated rod-like particles (2–5 μm), while $Na_2C_{14}H_8O_4$ presents as similar aggregated rod-like particles but with a larger size of 3–5 μm, and $Na_2C_{20}H_{10}N_2O_4$ presents as aggregated long rod-like particles (5–10 μm). These characterizations confirm the chemical structures and morphologies of the three conjugated carboxylate compounds.

To improve the performance of sodium carboxylates in NIBs, a highly conductive NrGO is mixed with Na-DCA to facilitate the electron and ion transfer in the anode. In addition, the large-surface-area and high-mechanical-strength NrGO can also accommodate the large volume change during repeated sodiation/de-sodiation process and form π-π interaction with Na-DCA, resulting in improved stability during long-term cycling. Na-DCA-NrGO was also characterized by XRD, FTIR, and SEM. As shown in Fig. 1a, the XRD pattern of Na-DCA-NrGO (red) shows a retained crystalline structure from Na-DCA (black) and obvious peaks overlapping at ~26° due to the presence of NrGO in the composite (Fig. S3b). The FTIR spectra in Fig. 1b shows maintained C=O asymmetric vibrations at ~1600 cm^{-1} and symmetric vibrations at 1394 cm^{-1}, and C=C ring stretching at ~1540 cm^{-1}. The SEM image of Na-DCA-NrGO (Fig. 1h) shows pulverized rods of Na-DCA interspersed with NrGO sheets. These characterizations confirm the chemical structure and morphology of the Na-DCA-NrGO composite.

To investigate their electrochemical performance in NIBs, the three conjugated carboxylate compounds were used as anode active materials with sodium metal as the counter electrode and 1.0 M $NaClO_4$ in ethylene carbonate (EC)/diethyl carbonate (DEC) as the electrolyte. As shown in Fig. 2a, the galvanostatic charge/discharge curves of $Na_2C_{14}H_8O_4$ exhibit a pair of sloping plateaus centered at ~0.5 V with a specific capacity of only 31 mAh g^{-1}, which is very similar to the electrochemical behaviors of carbon black (Fig. S4). The similar charge/discharge plateaus and slightly lower reversible capacity demonstrate that $Na_2C_{14}H_8O_4$ is electrochemically inactive as an anode in NIBs, and the attained capacity of the $Na_2C_{14}H_8O_4$ anode is mainly contributed by carbon black. In contrast, the galvanostatic charge/discharge curves of Na-DCA, shown in Fig. 2b, exhibit one pair of redox plateaus centered at ~0.48 V with a reversible capacity of 258.7 mAh g^{-1}, while $Na_2C_{20}H_{10}N_2O_4$ delivers a pair of redox plateaus centered at ~0.6 V with a lower reversible capacity of 114.5 mAh g^{-1} (Fig. 2c), demonstrating that the two N-containing sodium carboxylates are electrochemically active in NIBs. Compared to Na-DCA, the extended aromatic ring structure in $Na_2C_{20}H_{10}N_2O_4$ not only elevates the redox potential but also reduces the reversible capacities. The extended conjugation structure in $Na_2C_{20}H_{10}N_2O_4$ enhances the molecular weight of the organic electrode material but does not introduce any new redox-active sites to react with Na^+/electron, so the capacity of $Na_2C_{20}H_{10}N_2O_4$ is lower than that of Na-DCA. Additionally, the extended ring structures increase the solubility of $Na_2C_{20}H_{10}N_2O_4$ in the electrolyte, leading to fast capacity decay (Fig. 2f). Therefore, Na-DCA, the sodium carboxylate with two pyridine moieties, shows the most promising performance in NIBs among the three organic anode materials. Further investigation of the N-containing sodium carboxylate as an anode in NIBs is focused on Na-DCA. In the CV (Fig. S5a), one pair of cathodic and anodic peaks are observed at ~0.1 V and ~0.5 V, corresponding to redox plateaus centered at ~0.48 V in Fig. 2b. During the long-term cycling test (Fig. 2e), a reversible capacity of 124 mAh g^{-1} at 50 mA g^{-1} was achieved and retained after 200 cycles. The Coulombic efficiency of the long-term cycling was >98%. The contribution of carbon black to the reversible capacity of the Na-DCA anode was subsequently measured and found to exhibit a reversible capacity of 63 mAh g^{-1} (Fig. S4). This capacity was subtracted from the capacity from Na-DCA and is presented in Fig. S6. The rate capability of Na-DCA was measured from 20 mA g^{-1} to 2 A g^{-1}, as shown in Fig. S5b, and demonstrated reversible capacities of 312.2 mAh g^{-1} and 30.5 mAh g^{-1}, respectively. After the current density reduces back to 20 mA g^{-1}, a reversible capacity of 295.2 mAh g^{-1} can be retained, demonstrating robust reaction kinetics. However, Na-DCA loses 50% of its initial capacity at 50 mA g^{-1} after 200 cycles during the long-term cycling stability test owing to the high solubility of the active material in the electrolyte. To decrease its solubility and therefore improve the long-term cycling stability, two methods were employed: (1) π-π interaction between Na-DCA and NrGO; (2)

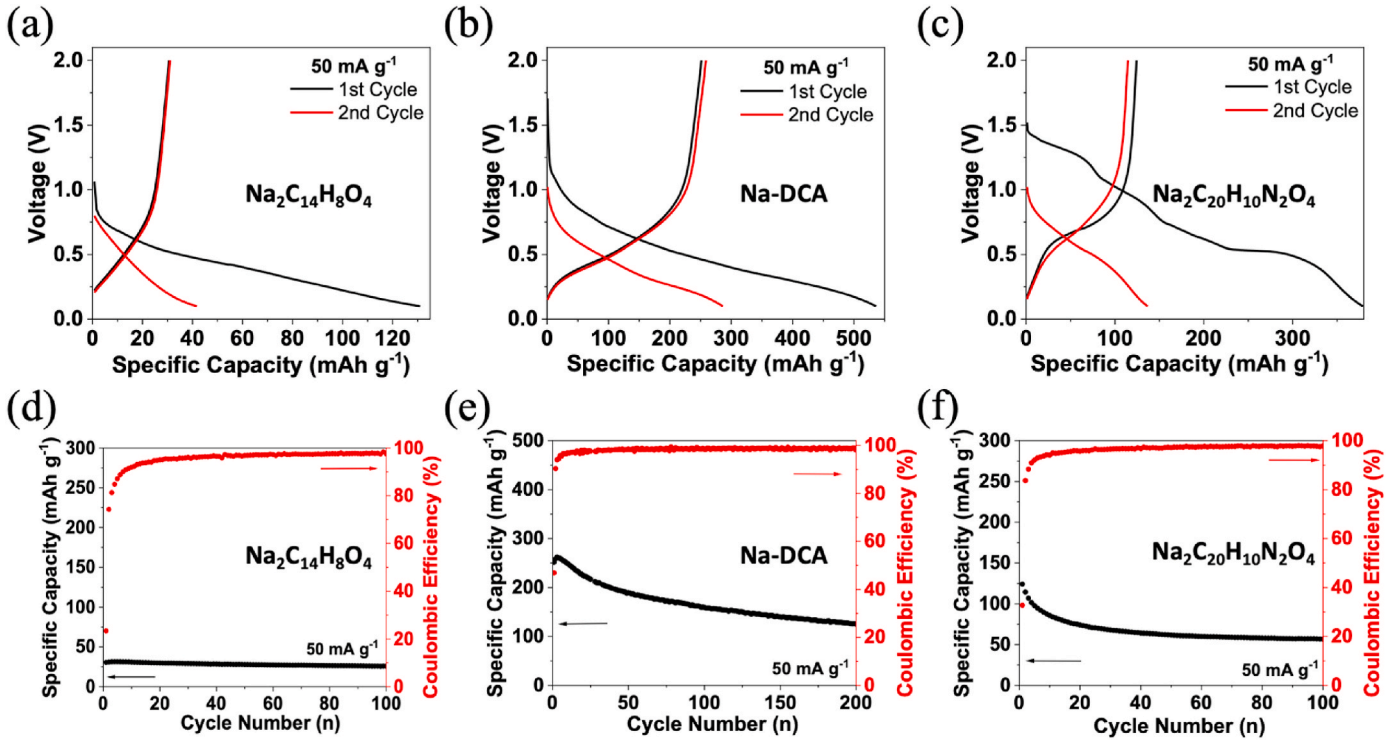

Fig. 2. Electrochemical performance of $Na_2C_{14}H_8O_4$, Na-DCA, and $Na_2C_{20}H_{10}N_2O_4$ in NIBs. (a–c) Galvanostatic charge-discharge curves; (d–e) De-sodiation capacity and Coulombic efficiency versus cycle number at the current density of 50 mA g^{-1}.

electrolyte optimization by tuning the concentration of the inorganic salt (perchlorate, $NaClO_4$) in the electrolyte, and thus the polarity and donor abilities of the electrolyte can be altered [37].

The electrochemical behaviors of Na-DCA-NrGO were assessed with sodium metal as the counter electrode and 1.0 M or 1.2 M $NaClO_4$-EC/DEC electrolyte in NIBs. The galvanostatic charge/discharge curves of Na-DCA-NrGO in 1.0 M $NaClO_4$-EC/DEC electrolyte, shown in Fig. S7a, exhibit one pair of redox plateaus centered at ~0.48 V with a reversible capacity of 339.8 mAh g^{-1}. The enhanced reversible capacity is attributed to the contribution by NrGO and the improved reaction kinetics. In the CV (Fig. S7b), there are one sharp cathodic peak at 0.1 V and one broad cathodic peak at ~0.45 V, while two broad and overlapping anodic peaks at ~0.45 V and ~0.7 V can also be observed, corresponding to the redox plateaus centered at ~0.48 V in Fig. S6a. During the long-term cycling tests (Fig. S7c), a reversible capacity of 186.51 mAh g^{-1} at 50 mA g^{-1} was retained after 200 cycles, demonstrating improved cycling stability. The Coulombic efficiency of the long-term cycling was close to 100%. The rate capability of Na-DCA-NrGO was measured from 20 mA g^{-1} to 1 A g^{-1} in Fig. S7d. A reversible capacity of 373.4 mAh g^{-1} is reduced to 89.7 mAh g^{-1} when the current density increases from 20 mA g^{-1} to 1 A g^{-1}. After the current density reduces back to 20 mA g^{-1}, a reversible capacity of 314.5 mAh g^{-1} is recovered, demonstrating excellent reaction kinetics. Although improved electrochemical performance is achieved for the Na-DCA-NrGO anode, obvious capacity loss can still be observed.

To further enhance its cycle life, electrolyte optimization via increasing the concentration of the ionic salt in the electrolyte was performed. By increasing the concentration of the electrolyte from 1.0 M to 1.2 M, an increase in cycling stability can be observed at the price of slightly lower reversible capacity. The galvanostatic charge/discharge

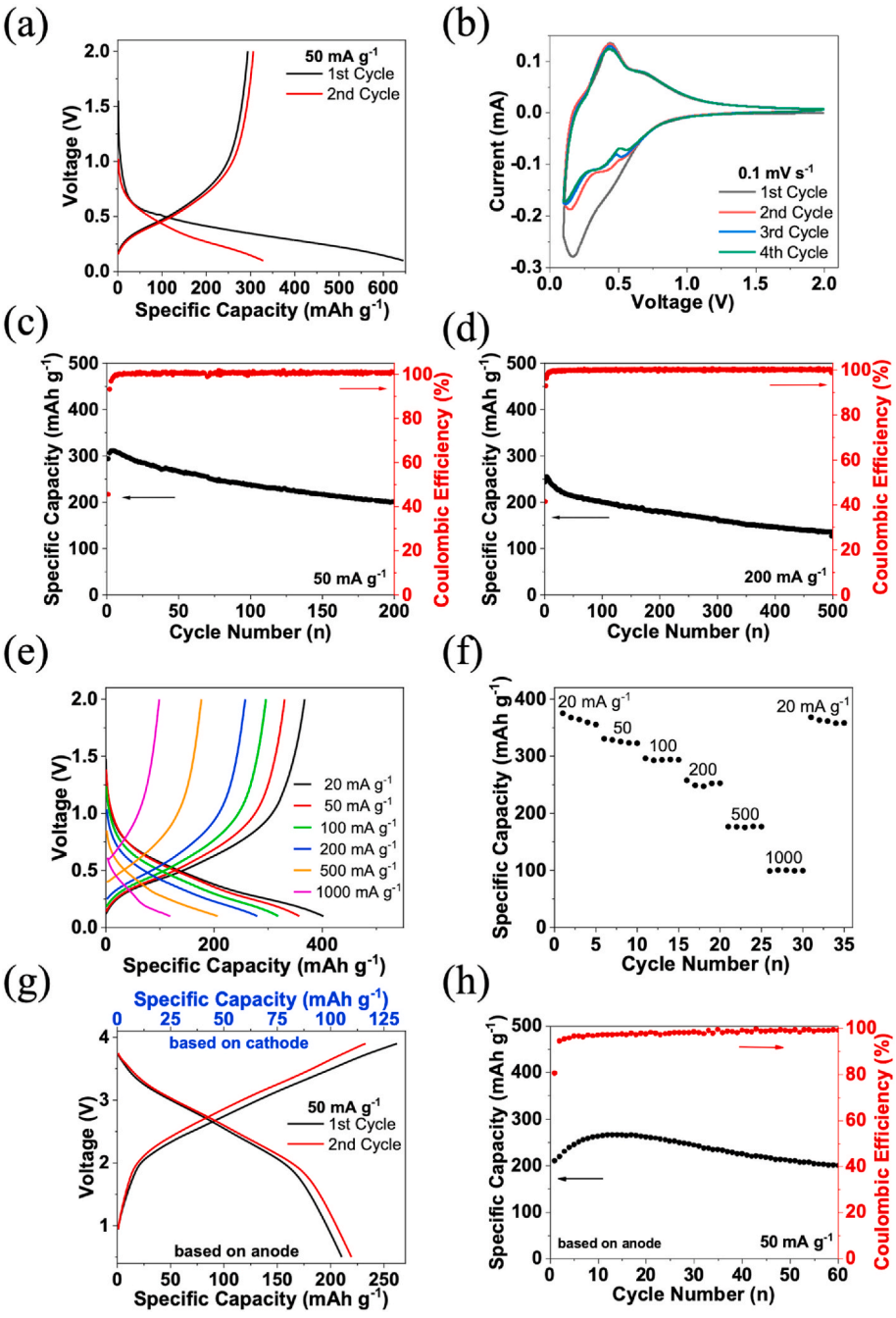

Fig. 3. Electrochemical performance and reaction kinetics of Na-DCA-NrGO (1.2 M) in NIBs. (a) Galvanostatic charge-discharge curves; (b) Cyclic voltammograms at 0.1 mV s^{-1}; (c) De-sodiation capacity and Coulombic efficiency versus cycle number at the current density of 50 mA g^{-1}; (d) De-sodiation capacity and Coulombic efficiency versus cycle number at the current density of 200 mA g^{-1}; (e) Galvanostatic charge-discharge curves at various current densities; (f) Rate performance at various current densities; Electrochemical performance of full cell Na-DCA-NrGO | PANI-NrGO (1.2 M). (g) Galvanostatic charge-discharge curves; (h) De-sodiation capacity based on the anode and Coulombic efficiency versus cycle number at the current density of 50 mA g^{-1}.

curves, shown in Fig. 3a, exhibit one pair of redox plateaus centered at ~0.48 V with a reversible capacity of 294.0 mAh g^{-1} in the first cycle. The reversible capacity increases to 310.9 mAh g^{-1} in a few cycles due to the initial activation process in the 1.2 M electrolyte. The contribution of NrGO to the reversible capacity was subsequently measured and found to exhibit a reversible capacity of 90 mAh g^{-1} (Fig. S8). The capacity was subtracted from the capacity from Na-DCA and is presented in Fig. S9. In the CV (Fig. 3b), the redox peaks in the 1.2 M electrolyte are slightly different from that in the 1.0 M electrolyte. The sharp and strong cathodic peak is at 0.15 V, while the strong anodic peak is at 0.45 V. In the long-term cycling tests (Fig. 3c–d), reversible capacities of 200 mAh g^{-1} at 50 mA g^{-1} and 126 mAh g^{-1} at 200 mA g^{-1} were retained after 200 cycles and 500 cycles, respectively, demonstrating excellent cycling stability. The Coulombic efficiency of the long-term cycling was close to 100%. The rate capability of Na-DCA-NrGO was measured from 20 mA g^{-1} to 1 A g^{-1}, as shown in Fig. 3e–f, and demonstrated reversible capacities of 375.0 mAh g^{-1} and 98.8 mAh g^{-1}, respectively. After the current density reduces back to 20 mA g^{-1}, a reversible capacity of 368.1 mAh g^{-1} can be recovered, demonstrating robust reaction kinetics. This result confirms that using highly conductive NrGO and a concentrated electrolyte are effective methods to improve the electrochemical performance of the Na-DCA anode in NIBs.

To further understand the electrochemical behavior of Na-DCA-NrGO in the 1.2 M electrolyte, galvanostatic intermittent titration technique (GITT) and electrochemical impedance spectroscopy (EIS) were employed to study the reaction kinetics. The equilibrium potentials obtained from GITT are shown in Fig. S10a. The charge/discharge equilibrium potentials of Na-DCA-NrGO are centered at 0.7 V/0.3 V with overpotentials of 52 mV and 46 mV at the charge and discharge plateaus, respectively. The small overpotentials confirm the fast reaction kinetics of Na-DCA-NrGO. Additionally, EIS was employed to evaluate the impedance evolution of the Na-DCA-NrGO anode upon cycling. Presented in Fig. S10b, the interfacial impedance of the fresh cell is ~280 Ω and slightly increases to ~300 Ω after 1 cycle. After 5, 10, and 20 cycles, the interfacial impedance was retained at ~300 Ω. The stable interfacial impedance from the 1st to 20th cycle demonstrates the stable solid electrolyte interphase (SEI) layer upon long-term cycling, which contributes to the stable cycle life. The GITT and EIS confirm fast reaction kinetics and the formation of a stable SEI layer of the Na-DCA-NrGO anode in NIBs. As a comparison, the reaction kinetics of Na-DCA in the 1.0 M electrolyte were also investigated by GITT and EIS. The equilibrium potentials obtained from GITT are shown in Fig. S11a. The charge/discharge equilibrium potentials remain centered at 0.7 V/0.3 V, respectively. However, the exhibited overpotentials are slightly larger, at 65 mV and 70 mV, indicating that the addition of NrGO and the increased electrolyte concentration aides in improving the reaction kinetics. Furthermore, EIS evaluated the impedance evolution of Na-DCA upon cycling. Shown in Fig. S11b, the interfacial impedance of the fresh cell is ~35 Ω and slightly increases to ~40 Ω after 1 cycle. With continued cycling, the interfacial impedance continues to increase from ~95 Ω after 5 cycles to ~135 Ω after 10 cycles, and finally ~185 Ω after 20 cycles. Though the interfacial impedance of Na-DCA in the 1.0 M electrolyte is lower than that of Na-DCA-NrGO in the 1.2 M electrolyte, the continuous increase of the interfacial impedance indicates the instability of the SEI layer, resulting in its rapid capacity loss and diminished cycle life. These results confirm that an improved carboxylate anode can be attained by adding NrGO and increasing the salt concentration of the electrolyte.

Since the Na-DCA-NrGO anode exhibits the best performance in NIBs, we further couple it with a p-type polymer cathode, polyaniline (PANI), to evaluate the performance of the all-organic full cell. Galvanostatic charge/discharge curves and cycle life for the PANI cathode are presented in Figs. S11a–b, showing a pair of slopping redox plateaus centered at 3.1 V with a reversible capacity of 138.5 mAh g^{-1} at 100 mA g^{-1} for 50 cycles. The full cell based on the Na-DCA-NrGO anode and the PANI cathode was cycled between 0.5 and 3.9 V. The galvanostatic charge/discharge curves in Fig. 3g exhibit one pair of slopping redox plateaus centered at ~2.8 V with a reversible capacity of 210.4 mAh, g^{-1} in the first cycle, and it quickly increases to 265.8 mAh g^{-1} after a few cycles (Fig. 3h). In the CV (Fig. S12a), two cathodic peaks at ~2.8 V and ~3.3 V and two side-by-side anodic peaks at ~2.9 V and ~3.0 V can be observed, corresponding to the redox plateaus centered at ~2.8 V in Fig. 3g. In the long-term cycling tests (Fig. 3h), a reversible capacity of 207.1 mAh g^{-1} at 50 mA g^{-1} based on the weight of the anode material was retained for 60 cycles. The Coulombic efficiency of the long-term cycling was >99%. The cycle life based on the weight of the cathode is also provided in Fig. S13. The rate capability of the full cell was measured from 20 mA g^{-1} to 2 A g^{-1}, as shown in Fig. S12b, and demonstrated reversible capacities of 259.4 mAh g^{-1} and 104.6 mAh g^{-1}, respectively. After the current density reduces back to 20 mA g^{-1}, a reversible capacity of 237.3 mAh g^{-1} can be recovered, demonstrating good reaction kinetics. These full cell results further confirm the robustness, stability, and excellent electrochemical performance of Na-DCA-NrGO in rechargeable sodium batteries.

In addition to studying the electrochemical performance, XRD, FTIR, and SEM were used to evaluate the molecular, crystalline, and morphological structures of the anode material, Na-DCA-NrGO, upon cycling. The *in-situ* XRD patterns in Fig. 4a show that the XRD peaks at 0.64, 0.73, 1.36, and 1.6° disappear during the first discharge, indicating phase transformation. The *ex-situ* XRD patterns of pristine and cycled Na-DCA-NrGO anodes in Fig. 4b, do not show changes to the crystalline structure, demonstrating that the initial phase transformation is reversible, and the crystalline structure is stable upon cycling. Additionally, *ex-situ* XRD measurements (Fig. S14) for the first charge process at various charge stages were performed, however, these patterns do not show any discernible changes. The difference in the 2-theta degree of the *in-situ* and *ex-situ* XRD patterns is owing to the different wavelength of the X-ray beam ($\lambda = 0.1173$ Å and $\lambda = 1.5418$ Å) used for the tests. These *ex-situ* XRD tests were performed on thick electrodes, prepared with polytetrafluoroethylene (PTFE) as the binder, which presents with a strong peak at 18.2°. The PTFE peak does not change in the pristine and cycled electrodes. FTIR was also used to study the molecular structure change of Na-DCA-NrGO upon cycling. As shown in Fig. 4c, the FTIR peaks for pristine and cycled Na-DCA-NrGO do not show visible changes before and after cycling, demonstrating that the molecular structures of Na-DCA and NrGO are well maintained after the sodiation/de-sodiation process. Additionally, to explore and confirm the proposed redox mechanism, *ex-situ* Raman was employed to confirm the active sites in Na-DCA during charge/discharge processes. Presented in Fig. S15, the *ex-situ* Raman spectra show that the Raman peaks for the carbonyl group and pyridine group in Na-DCA are disappeared when it is discharged (0.5V and 0.1V). Upon charging to 2V, the carbonyl and pyridine peaks re-appear, demonstrating a reversible electrochemical reaction between both the carbonyl and pyridine groups and Na ions. SEM is further employed to gain insights into the morphology changes of pristine and cycled Na-DCA-NrGO anodes. Fig. 4d–g shows that several pores (red circles) are generated on the anode surface after 1, 10, and 20 cycles due to the large volume changes caused by repeated sodiation/de-sodiation processes. The obvious morphology changes lead to the gradual capacity loss upon long-term cycling. In comparison, pristine and cycled Na-DCA anodes were evaluated using FTIR and SEM to determine the stabilizing effects of NrGO and the higher concentration electrolyte. Presented in Fig. S16a, the FTIR for pristine and cycled Na-DCA does not show significant changes before and after cycling until the 20th cycle. Demonstrating that the molecular structure of Na-DCA is preserved after repeated sodiation/de-sodiation processes but does start to deteriorate with continued cycling. To further understand these structural changes and examine the morphology changes during cycling, SEM was employed. Figs. S16b–e show that with increased cycling, numerous large cracks are generated on the anode surface after 1, 10, and 20 cycles. These significant morphology changes are caused by repeated sodiation/de-sodiation

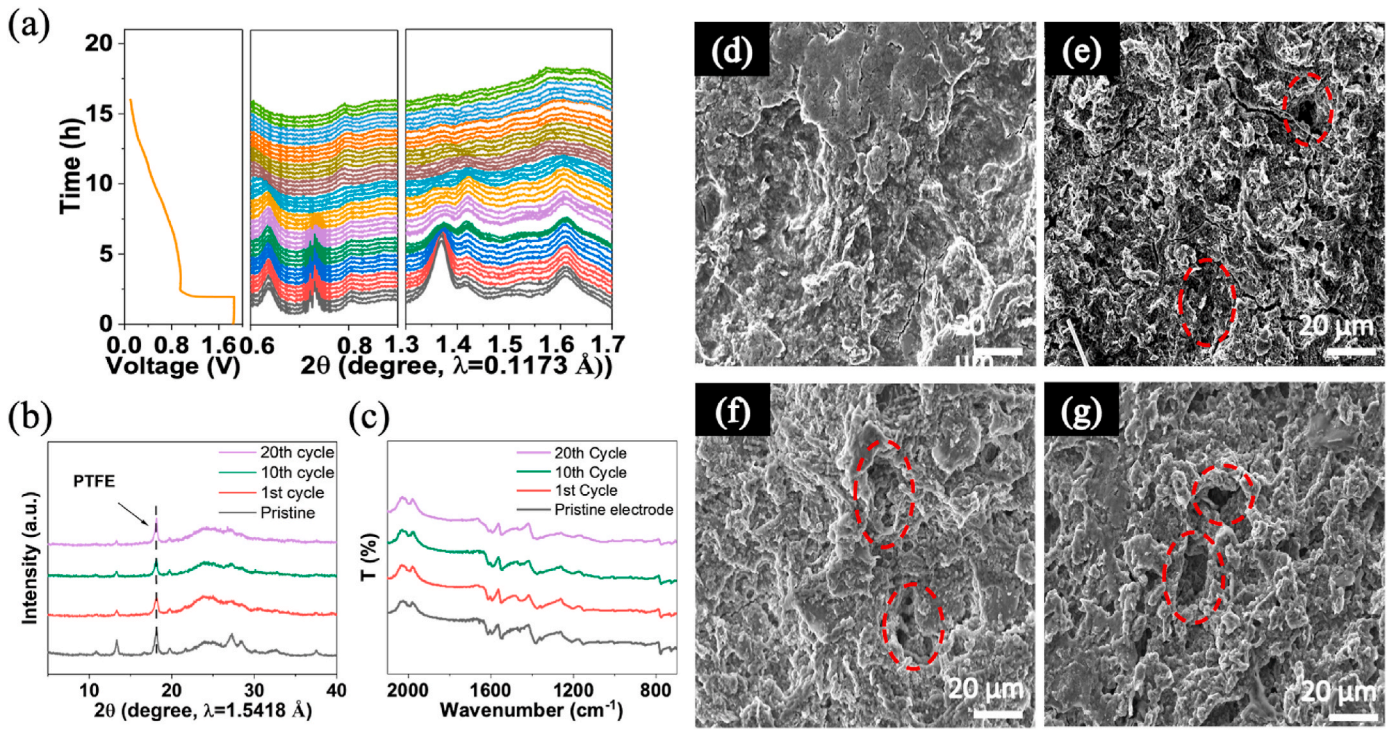

Fig. 4. Characterizations of pristine and cycled Na-DCA-NrGO electrodes. (a) *in-situ* XRD patterns of anode material, (b) XRD patterns of anode material, pristine, and cycled electrodes; (c) FTIR spectra of anode material, pristine, and cycled electrodes; SEM images with scale bar of 20 μm of (d) Pristine electrode; and Cycled electrodes after (e) 1 cycle with pores measuring 9.125 μm (top) and 10.83 μm (bottom) circled; (f) 10 cycles with pores measuring 8.137 μm (top) and 8.176 μm (bottom) circled; and (g) 20 cycles with pores measuring 7.234 μm (top) and 10.60 μm (bottom) circled.

processes and lead to the rapid capacity loss during long-term cycling. These results confirm that the crystalline and molecular structures of Na-DCA are stable upon cycling, but the morphology changes caused by the volume expansion/shrinkage during the sodiation/de-sodiation process results in the capacity decay of Na-DCA-NrGO. Therefore, further performance optimization can be achieved by accommodating the large volume change of sodium carboxylate anodes in the long-term cycling.

In this work, we exploited and expanded the structure design strategy of conjugated sodium carboxylates to obtain high-capacity organic anodes for NIBs. As shown in Fig. 5a and Fig. 5b, the conventional

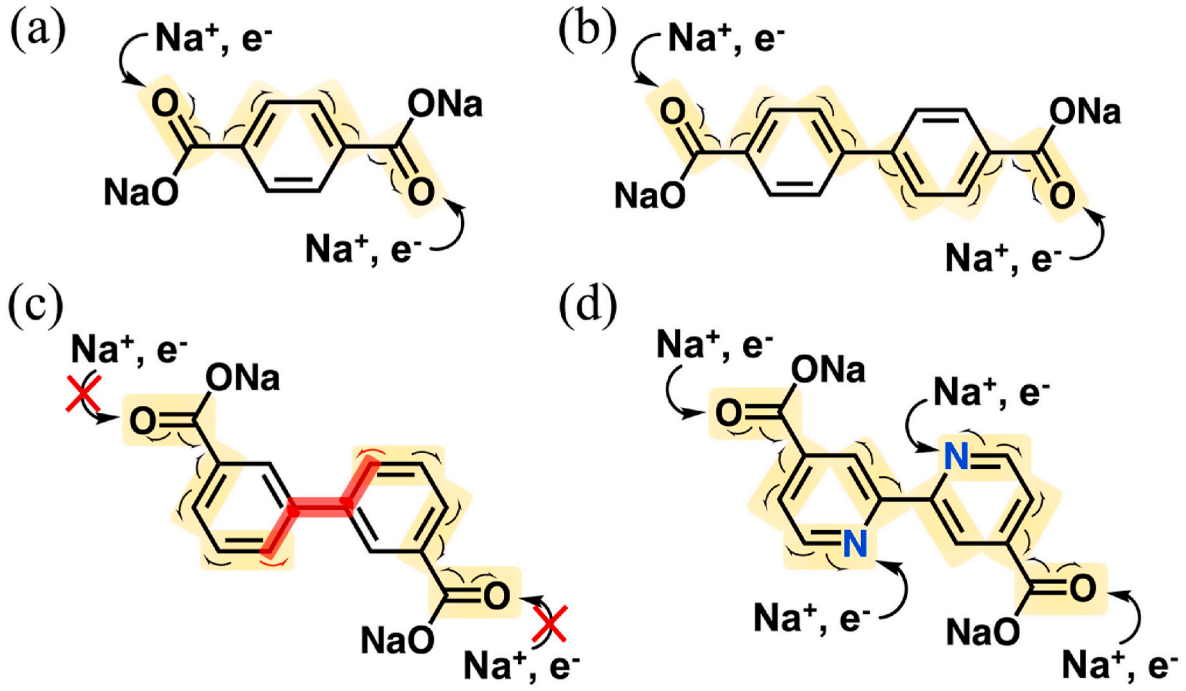

Fig. 5. Structure design strategy for high-capacity carboxylate anodes in NIBs. (a) Sodium terephthalate; (b) 4,4′-biphenyldicarboxylic acid disodium salt; (c) Biphenyl-3,3′-dicarboxylic acid disodium salt ($Na_2C_{14}H_8O_4$); (d) Na-DCA.

sodium carboxylate anodes contain a pair of carboxylate groups on the *para* position of the benzene ring, where the active centers (C=O) are connected by a conjugated structure as the highlighted yellow region. When the O in the carbonyl groups react with Na-ions and electrons, the carbon-carbon and carbon-oxygen double bonds are cleaved and rebonded to form a stable product. In general, to obtain an electrochemically active OEM, two or more active centers should be connected by a fully conjugated structure, which consists of strictly alternating carbon-carbon double and single bonds. However, the two active centers (C=O) in $Na_2C_{14}H_8O_4$ are not connected by a fully conjugated structure as shown in Fig. 5c. When reacting with Na-ions and electrons, sodiated $Na_2C_{14}H_8O_4$ cannot form a stable product (Scheme 1b), and thus it is electrochemically inactive. To form a fully conjugated structure to connect active centers in $Na_2C_{14}H_8O_4$, the carbons on the *para* position of the benzene rings can be replaced by N to create extra active centers to alter the conjugation structure. For instance, Na-DCA with N on the *para* positions contains four active centers, two carboxylate groups, and two N in the pyridine moieties. When two N in the pyridine moieties react with Na^+ and electrons, it triggers the rearrangement of the carbon-carbon double and single bonds (Scheme 1e), which reconnects the two carboxylate groups by a fully conjugated structure. All the active centers in Na-DCA are connected by strictly alternating carbon-carbon double and single bonds during the redox reaction, and Na-DCA demonstrates a high-capacity organic anode as evidenced in this work. Therefore, we not only revisit the general structure design strategy of connecting active centers by strictly alternating carbon-carbon double and single bonds to provide organic carboxylate anodes but also expand the strategy to introduce multi-active centers into inactive sodium carboxylates to tailor the conjugation structure in sodium carboxylates to form high-capacity and low-voltage organic carboxylate anodes for sustainable NIBs.

4. Conclusions

In conclusion, this work unravels the substitution rule of the N heteroatom and extended conjugation structure in the aromatic sodium carboxylates to obtain high-capacity organic anode materials for NIBs. Among the three conjugated sodium carboxylates studied in this work, Na-DCA with two pyridine moieties and two carboxylate groups exhibits the best electrochemical performance in NIBs due to the formation of stable resonance products and the four-electron/Na^+ redox mechanism. It provides a structure design strategy of integrating carboxylate groups and pyridine moieties to convert an electrochemically inactive carboxylate compound ($Na_2C_{14}H_8O_4$) into an active OEM (Na-DCA). Introducing N onto the *para* position of the benzene ring bearing carboxylate groups can significantly promote the thermodynamic reaction and enable the electrochemical redox reaction of aromatic sodium carboxylates in NIBs. Further extending the conjugation structure of Na-DCA provides $Na_2C_{20}H_{10}N_2O_4$, but it showed a decreased specific capacity and an increased redox potential. To improve the performance of Na-DCA, the large-surface-area and highly conductive NrGO and a 1.2 M $NaClO_4$-EC/DEC electrolyte are employed to enhance the electrode conductivity, mitigate the dissolution of Na-DCA and its sodiated product in the electrolyte, as well as accommodate the large volume change during sodiation/de-sodiation. The Na-DCA-NrGO composite displayed excellent electrochemical performance in terms of high capacity and long cycle life. GITT and EIS tests further confirm the superior reaction kinetics and stable interfacial resistance, while FTIR and XRD results demonstrate the stable molecular and crystalline structures of Na-DCA upon cycling. Pairing the Na-DCA-NrGO anode material with a PANI cathode in a full cell continued to demonstrate its potential in enabling a high-performance all-organic battery. Therefore, this work paves the way for developing conjugated carboxylate anodes for stable and sustainable NIBs.

CRediT authorship contribution statement

Kathryn Holguin: Methodology, Validation, Investigation, Data curation, Writing – original draft. **Kaiqiang Qin:** Methodology, Validation, Investigation, Data curation. **Ethan Phillip Kamphaus:** Methodology, Software, Formal analysis, Investigation, Data curation. **Fu Chen:** Methodology, Validation, Investigation. **Lei Cheng:** Methodology, Writing – review & editing, Supervision, Funding acquisition. **Gui-Liang Xu:** Methodology, Writing – review & editing, Supervision, Funding acquisition. **Khalil Amine:** Supervision, Funding acquisition. **Chao Luo:** Conceptualization, Methodology, Writing – review & editing, Supervision, Project administration, Funding acquisition.

Declaration of competing interest

The authors declare that they have no known competing financial interests or personal relationships that could have appeared to influence the work reported in this paper.

Acknowledgments

This work was supported by the US National Science Foundation Award No. 2000102 and the George Mason University, College of Science Postdoctoral Fellowship. The authors also acknowledge the support from the George Mason University Quantum Science & Engineering Center. The solid-state 500 MHz NMR spectrometer at University of Maryland was supported by the NSF MRI grant (NSF-1726058). Research at the Argonne National Laboratory was funded by the US Department of Energy (DOE), Vehicle Technologies Office. Support from T. Duong of the US DOE's Office of Vehicle Technologies Program is gratefully acknowledged. Ms. Motahareh Mohammadiroudbari is acknowledged for her ongoing support and technical assistance with electrochemical tests.

Appendix A. Supplementary data

Supplementary data to this article can be found online at https://doi.org/10.1016/j.jpowsour.2022.231383.

References

[1] V. Palomares, P. Serras, I. Villaluenga, K.B. Hueso, J. Carretero-González, T. Rojo, Na-ion batteries, recent advances, and present challenges to become low-cost energy storage systems, Energy Environ. Sci. 5 (2012) 5884–5901.
[2] M.D. Slater, D. Kim, E. Lee, C.S. Johnson, Sodium-ion batteries, Adv. Funct. Mater. 23 (2013) 947–958.
[3] A. Zhou, W. Cheng, W. Wang, Q. Zhao, J. Xie, W. Zhang, H. Gao, L. Xue, J. Li, Hexacyanoferrate-type prussian blue analogs: principles and advances toward high-performance sodium and potassium ion batteries, Adv. Energy Mater. 11 (2021) 2000943.
[4] H. Pan, Y.S. Hu, L. Chen, Room-temperature stationary sodium-ion batteries for large-scale electric energy storage, Energy Environ. Sci. 6 (2013) 2338–2360.
[5] N. Yabuuchi, K. Kubota, M. Dahbi, S. Komaba, Research development on sodium-ion batteries, Chem. Rev. 114 (2014) 11636–11682.
[6] L. Li, Y. Zheng, S. Zhang, J. Yang, Z. Shao, Z. Guo, Recent progress on sodium ion batteries: potential high-performance anodes, Energy Environ. Sci. 11 (2018) 2310–2340.
[7] J.J. Shea, C. Luo, Organic electrode materials for metal ion batteries, ACS Appl. Mater. Interfaces 12 (2020) 5361–5380.
[8] Y. Lu, Q. Zhang, L. Li, Z. Niu, J. Chen, Design strategies toward enhancing the performance of organic electrode materials in metal-ion batteries, Inside Chem. 4 (2018) 2786–2813.
[9] K. Qin, J. Huang, K. Holguin, C. Luo, Recent advances in developing organic electrode materials for multivalent rechargeable batteries, Energy Environ. Sci. 13 (2020) 3950–3992.
[10] K. Holguin, M. Mohammadiroudbari, K. Qin, C. Luo, Organic electrode materials for non-aqueous, aqueous, and all-solid-state Na-ion batteries, J. Mater. Chem. 9 (2021) 19083–19115.
[11] Q. Zhao, J. Wang, Y. Lu, Y. Li, G. Liang, J. Chen, Oxocarbon salts for fast rechargeable batteries, Angew. Chem. Int. Ed. 55 (2016) 12528–12532.
[12] K. Qin, K. Holguin, M. Mohammadiroudbari, C. Luo, A conjugated tetracarboxylate anode for stable and sustainable Na-ion batteries, Chem. Commun. 57 (2021) 2360–2363.

[13] E. Castillo-Martínez, J. Carretero-González, M. Armand, Polymeric Schiff bases as low-voltage redox centers for sodium-ion batteries, Angew. Chem. Int. Ed. 53 (2014) 5341–5345.
[14] M. López-Herraiz, E. Castillo-Martínez, J. Carretero-González, J. Carrasco, T. Rojo, M. Armand, Oligomeric-Schiff bases as negative electrodes for sodium ion batteries: unveiling the nature of their active redox centers, Energy Environ. Sci. 8 (2015) 3233–3241.
[15] C. Luo, O. Borodin, X. Ji, S. Hou, K.J. Gaskell, X. Fan, J. Chen, T. Deng, R. Wang, J. Jiang, C. Wang, Azo compounds as a family of organic electrode materials for alkali-ion batteries, Proc. Natl. Acad. Sci. U.S.A. 115 (2018) 2004–2009.
[16] H. Zhao, J. Wang, Y. Zheng, J. Li, X. Han, G. He, Y. Du, Organic thiocarboxylate electrodes for a room-temperature sodium-ion battery delivering an ultrahigh capacity, Angew. Chem. Int. Ed. 129 (2017) 15536–15540.
[17] K. Sakaushi, E. Hosono, G. Nickerl, T. Gemming, H. Zhou, S. Kaskel, J. Eckert, Aromatic porous-honeycomb electrodes for a sodium-organic energy storage device, Nat. Commun. 4 (2013) 1485.
[18] S. Lee, G. Kwon, K. Ku, K. Yoon, S.K. Jung, H.D. Lim, K. Kang, Recent progress in organic electrodes for Li and Na rechargeable batteries, Adv. Mater. 30 (2018) 1704682.
[19] S. Lee, J. Hong, K. Kang, Redox-active organic compounds for future sustainable energy storage system, Adv. Energy Mater. 10 (2020) 2001445.
[20] M. Mao, C. Luo, T.P. Pollard, S. Hou, T. Gao, X. Fan, C. Cui, J. Yue, Y. Tong, G. Yang, T. Deng, M. Zhang, J. Ma, L. Suo, O. Borodin, C. Wang, A pyrazine-based polymer for fast-charge batteries, Angew. Chem. Int. Ed. 58 (2019) 17820–17826.
[21] R. Shi, L. Liu, Y. Lu, C. Wang, Y. Li, L. Li, Z. Yan, J. Chen, Nitrogen-rich covalent organic frameworks with multiple carbonyls for high-performance sodium batteries, Nat. Commun. 11 (2020) 178.
[22] T. Sun, J. Xie, W. Guo, D.S. Li, Q. Zhang, Covalent–organic frameworks: advanced organic electrode materials for rechargeable batteries, Adv. Energy Mater. 10 (2020) 1904199.
[23] C. Luo, X. Fan, Z. Ma, T. Gao, C. Wang, Self-healing chemistry between organic material and binder for stable sodium-ion batteries, Inside Chem. 3 (2017) 1050–1062.
[24] Y. Wu, Y. Chen, M. Tang, S. Zhu, C. Jiang, S. Zhuo, C. Wang, A highly conductive conjugated coordination polymer for fast-charge sodium-ion batteries: reconsidering its structures, Chem. Commun. 55 (2019) 10856–10859.
[25] M.S. Kim, M. Lee, M.J. Kim, Y.K. Jeong, J.K. Park, S.M. Paek, Molecular engineering of covalent organic nanosheets for high-performance sodium-ion batteries, J. Mater. Chem. 8 (2020) 17790–17799.
[26] S. Wu, W. Wang, M. Li, L. Cao, F. Lyu, M. Yang, Z. Wang, Y. Shi, B. Nan, S. Yu, Z. Sun, Y. Liu, Z. Lu, Highly durable organic electrode for sodium-ion batteries via a stabilized α-C radical intermediate, Nat. Commun. 7 (2016) 13318.
[27] M. Lee, J. Hong, J. Lopez, Y. Sun, D. Feng, K. Lim, W.C. Chueh, M.F. Toney, Y. Cui, Z. Bao, High-performance sodium–organic battery by realizing four-sodium storage in disodium rhodizonate, Nat. Energy 2 (2017) 861–868.
[28] T.B. Schon, B.T. McAllister, P.F. Li, D.S. Seferos, The rise of organic electrode materials for energy storage, Chem. Soc. Rev. 45 (2016) 6345–6404.
[29] B. Häupler, A. Wild, U.S. Schubert, Carbonyls: powerful organic materials for secondary batteries, Adv. Energy Mater. 5 (2015) 1402034.
[30] Y. Xu, M. Zhou, Y. Lei, Organic materials for rechargeable sodium-ion batteries, Mater. Today 21 (2018) 60–78.
[31] Q. Zhao, Y. Lu, J. Chen, Advanced organic electrode materials for rechargeable sodium-ion batteries, Adv. Energy Mater. 7 (2017) 1601792.
[32] T. Sun, J. Xie, W. Guo, D.S. Li, Q. Zhang, Disodium terephthalate (Na2C8H4O4) as high performance anode material for low-cost room-temperature sodium-ion battery, Adv. Energy Mater. 2 (2012) 962–965.
[33] A.V. Desai, R.E. Morris, A.R. Armstrong, Advances in organic anode materials for Na-/K-ion rechargeable batteries, ChemSusChem 13 (2020) 4866–4884.
[34] P. Poizot, J. Gaubicher, S. Renault, L. Dubois, Y. Liang, Y. Yao, Opportunities and challenges for organic electrodes in electrochemical energy storage, Chem. Rev. 120 (2020) 6490–6557.
[35] C. Luo, G.L. Xu, X. Ji, S. Hou, L. Chen, F. Wang, J. Jiang, Z. Chen, Y. Ren, K. Amine, C. Wang, Reversible redox chemistry of azo compounds for sodium-ion batteries, Angew. Chem. Int. Ed. 57 (2018) 2879–2883.
[36] S. Muench, A. Wild, C. Friebe, B. Häupler, T. Janoschka, U.S. Schubert, Polymer-based organic batteries, Chem. Rev. 116 (2016) 9438–9484.
[37] C. Luo, J. Wang, X. Fan, Y. Zhu, F. Han, L. Suo, C. Wang, Roll-to-roll fabrication of organic nanorod electrodes for sodium ion batteries, Nano Energy 13 (2015) 537–545.
[38] C. Zhang, Y. Xu, K. He, Y. Dong, H. Zhao, L. Medenbach, Y. Wu, A. Balducci, T. Hannappel, Y. Lei, Polyimide@Ketjenblack composite: a porous organic cathode for fast rechargeable potassium-ion batteries, Small 16 (2020) 2002953.
[39] J. Hong, M. Lee, B. Lee, D.-H. Seo, C.B. Park, K. Kang, Biologically inspired pteridine redox centers for rechargeable batteries, Nat. Commun. 5 (2014) 5335.
[40] W. Luo, M. Allen, V. Raju, X. Ji, An organic pigment as a high-performance cathode for sodium-ion batteries, Adv. Energy Mater. 4 (2014) 1400554.
[41] X. Han, G. Qing, J. Sun, T. Sun, How many lithium ions can be inserted onto fused C6 aromatic ring systems? Angew. Chem. Int. Ed. 51 (2012) 5147–5151.
[42] Y. Shan, Y. He, N. Yang, X. Zhu, H. Liu, H. Jiang, C. Li, Regulating steric hindrance in redox-active porous organic frameworks achieves enhanced sodium storage performance, Small 18 (2022) 2270004.
[43] Y. Shan, Y. He, Y. Gu, Y. Sun, N. Yang, H. Jiang, F. Wang, C. Li, D.-E. Jiang, H. Liu, X. Zhu, S. Dai, Sodium storage in triazine-based molecular organic electrodes: the importance of hydroxyl substituents, Chem. Eng. J. 430 (2022) 133055.
[44] N. Yang, Y. Gu, Y. Shan, C. Tian, L. Yang, H. Jiang, H. Liu, X. Zhu, S. Dai, Dual rate-modulation approach for the preparation of crystalline covalent triazine frameworks displaying efficient sodium storage, ACS Macro Lett. 11 (2022) 60–65.
[45] C. Wang, Y. Xu, Y. Fang, M. Zhou, L. Liang, S. Singh, H. Zhao, A. Schober, Y. Lei, Extended π-conjugated system for fast-charge and -discharge sodium-ion batteries, J. Am. Chem. Soc. 137 (2015) 3124–3130.
[46] A. Abouimrane, W. Weng, H. Eltayeb, Y. Cui, J. Niklas, O. Poluektov, K. Amine, Sodium insertion in carboxylate-based materials and their application in 3.6 V full sodium cells, Energy Environ. Sci. 5 (2012) 9632–9638.